ADVANCED MATERIALS
www.advmat.de

Fiber Optic-Mediated Type I Photodynamic Therapy of Brain Glioblastoma Based on an Aggregation-Induced Emission Photosensitizer

Wenguang Zhang, Miaomiao Kang, Xue Li, Yinzhen Pan, Zhuorong Li, Yibin Zhang, Changrui Liao, Gaixia Xu, Zhijun Zhang, Ben Zhong Tang,* Zhourui Xu,* and Dong Wang**

Glioblastoma (GBM) is one of the most lethal human malignancies. The current standard-of-care is highly invasive with strong toxic side effects, leading to poor prognosis and high mortality. As a safe and effective clinical approach, photodynamic therapy (PDT) has emerged as a suitable option for GBM. Nevertheless, its implementation is significantly impeded by the limits of light penetration depth and the firm reliance on oxygen. To overcome these challenges, herein, a promising strategy that harnesses a modified optical fiber and less oxygen-dependent Type I aggregation-induced emission (AIE) photosensitizer (PS) is developed for the first time to realize in vivo GBM treatments. The proposed AIE PS, namely TTTMN, characterized by a highly twisted molecular architecture and a bulky spacer, exhibits enhanced near-infrared emission and strong production of hydroxyl and superoxide radicals at the aggregated state, thus affording efficient fluorescence imaging-guided PDT once formulated into nanoparticles. The inhibition of orthotopic and subcutaneous GBM xenografts provides compelling evidence of the treatment efficacy of Type I PDT irradiated through a tumor-inserted optical fiber. These findings highlight the substantially improved therapeutic outcomes achieved through fiber optic-mediated Type I PDT, positioning it as a promising therapeutic modality for GBM.

1. Introduction

Glioblastomas (GBMs), classified as high-grade malignancies (Grade IV WHO), stand as the most prevalent primitive brain tumors in adults, with an annual incidence of 5 cases per 100 000 individuals.[1] The current standard-of-care relies on maximal, safe surgical resection of the tumor, followed by complementary radiotherapy and chemotherapy.[2] However, GBMs exhibit aggressive and infiltrative growth patterns, with microscopic extension into normal brain parenchyma, which poses significant challenges for surgical removal, particularly in eloquent or vital brain regions.[3] Radiotherapy and chemotherapy, although effective, impose additional physical burdens and undermine the patient's immune system.[4] Therefore, GBMs are always associated with a poor prognosis and impaired quality of life, resulting in a 2-year survival rate of 27%.[5] Fortunately, the emergence of photodynamic therapy (PDT), in which

W. Zhang, Y. Zhang, G. Xu, Z. Xu
School of Biomedical Engineering
Shenzhen University Medical School
Shenzhen University
Shenzhen, Guangdong 518055, P. R. China
E-mail: xuzhouray@szu.edu.cn

M. Kang, X. Li, Y. Pan, Z. Zhang, B. Z. Tang, D. Wang
Center for AIE Research
Guangdong Provincial Key Laboratory of New Energy Materials Service Safety
College of Materials Science and Engineering
Shenzhen University
Shenzhen 518060, P. R. China
E-mail: zhijunzhang@szu.edu.cn; tangbenz@cuhk.edu.cn; wangd@szu.edu.cn

The ORCID identification number(s) for the author(s) of this article can be found under https://doi.org/10.1002/adma.202410142

DOI: 10.1002/adma.202410142

Z. Li, C. Liao
Shenzhen Key Laboratory of Photonic Devices and Sensing Systems for Internet of Things
Guangdong and Hong Kong Joint Research Centre for Optical Fiber Sensors
State Key Laboratory of Radio Frequency Heterogeneous Integration
Shenzhen University
Shenzhen 518060, P. R. China

Z. Li, C. Liao
Shenzhen Key Laboratory of Ultrafast Laser Micro/Nano Manufacturing
Key Laboratory of Optoelectronic Devices and Systems of Ministry of Education/Guangdong Province
College of Physics and Optoelectronic Engineering
Shenzhen University
Shenzhen 518060, P. R. China

B. Z. Tang
School of Science and Engineering
Shenzhen Institute of Aggregate Science and Technology
The Chinese University of Hong Kong
Shenzhen, Guangdong 518172, P. R. China

the reactive oxygen species (ROS) generated by photosensitizers (PSs) upon light irradiation is utilized to destroy targeted cells, has brought new hope to the treatment of GBMs.[6] Its remarkable attributes, such as minimal invasiveness, low toxicity, precise spatiotemporal selectivity, and ease of operation, effectively meet the demands of GBMs treatment, potentially representing a significant breakthrough in combating this formidable disease.[7]

Despite the great promise of PDT, its treatment efficacy in GBMs is hindered by light extinction in tissues and conflicts with the oxygen-consuming nature of PSs in hypoxic tumor microenvironments.[8] Over the past decade, research has focused on overcoming light penetration depth by developing long-wavelength PSs activated by either one-photon or two-photon processes.[9] However, even with light in the second near-infrared window (1000–1700 nm), best for light-based theranostics, the maximum penetration depth reported so far is only 25 mm,[10] which falls short of being able to penetrate through the skin, skull, and muscle layers, highlighting the need for further advancements in light delivery.[11] Another critical challenge is addressing the hypoxic environment within tumors during PDT.[12] Various oxygenation strategies, including oxygen delivery and in situ oxygen generation, have been explored to counteract the effects of hypoxia on PDT efficacy.[13] Although these strategies demonstrated potential in alleviating tumor hypoxia, challenges such as the intricate nanocomposite design, batch-to-batch variability, and demanding reaction conditions, pose significant hurdles in ensuring the safety, consistency, and clinical viability of PDT.[14] Thus, implementing PDT in GBM treatment remains a distant goal and mission impossible.

Fortunately, the advent of fiber optic technology has injected new vitality into PDT.[15] Optical fiber, known for its lossless light transmission, hair-like footprints, and flexibility, can be easily and non-invasively inserted into tumor lesions, thereby circumventing light attenuation in biological tissues and enabling internal tumor irradiation.[16] Building on this foundation, another key issue is how to effectively exert the photodynamic effects within hypoxic conditions. In recent years, Type I PSs that can either recycle oxygen or operate without oxygen to generate superoxide anion ($O_2^{\bullet-}$) and hydroxyl radical ($^{\bullet}OH$) have garnered significant attention.[17] Notably, $^{\bullet}OH$ with the strongest oxidizability and cytotoxicity compared to other radicals, makes Type I PSs even more prominent in PDT.[18] So far, Type I PSs with aggregation-induced emission (AIE) characteristics stand out as ideal choices for GBMs treatment.[19] Type I AIE PSs not only possess superior biocompatibility over inorganic materials but also exhibit AIE and aggregation-enhanced intersystem crossing (AIE-ISC) features, making them particularly effective when used in their aggregated state within physiological environments and facilitating fluorescence imaging-guided PDT.[20] Evidently, exploring advanced photodynamic protocols that combine Type I AIE PSs and optical fibers represents an appealing yet unresolved task in advancing GBM treatment.

In this contribution, we report, for the first time, the fiber optic-mediated Type I PDT for combating brain GBMs in vivo using a prominent AIE PS, namely TTTMN (**Scheme 1**). Attributed to the highly twisted architecture and prominent donor-acceptor (D–A) relationship, TTTMN exhibits remarkable production rates of $O_2^{\bullet-}$ and $^{\bullet}OH$ with NIR emission in the aggregated state. Theoretical calculations reveal the multi-channel transitions between the lowest singlet state (S_1) and the isoenergetic triplet states (T_n) with high SOC values, which support efficient ISC processes for photodynamic effect. Once formulated into nanoparticles (NPs) and modified with angiopep-2 (Ang2), TTTMN NPs-Ang2 can efficiently penetrate the blood-brain barrier (BBB) and selectively target GBMs. The outstanding therapeutic efficacy in vivo is further achieved after laser irradiation through a modified optical fiber, which can efficiently diffuse laser light in situ. With the challenges of biological light barriers and hypoxia being seriously considered and addressed, it is believed that the proposed photodynamic protocols would open up new avenues for treating GBMs and advancing their clinical application.

2. Results and Discussion

2.1. Molecular Design and Photophysical Property Studies

The compound TTTMN is designed with a typical D–A structure incorporating various core components: a triphenylamine (TPA) moiety working as an electron donor, thiophene serving as an additional electron donor and π-bridge, and two cyano units serving as electron acceptors. This configuration results in a strong D–A strength with extended conjugation, facilitating ROS generation and leading to a bathochromic-shift absorption and emission. The twisted conformation of the TPA moiety is crucial for activating radiative channels in the aggregate state by effectively inhibiting intermolecular $\pi-\pi$ stacking. The incorporation of tetraphenylethylene (TPE) provides abundant molecular rotors, further suppressing the fluorescence quenching effect of TTTMN at aggregated state. These structural characteristics contribute to the distinct AIE characteristics of TTTMN. In addition, the alkyl chain on TPA moiety offers additional spatial hindrance, which can further increase the intermolecular distance and resist $\pi-\pi$ stacking. Furthermore, considering the strong electron-donating ability of TPA and the significant electron deficiency of two cyano units, highly efficient ROS production and electron transfer behaviors are expected, promoting the generation of Type I ROS. Moreover, due to the strength of the D-A compound and the extended conjugation provided by a thiophene unit and a carbon-carbon double bond, emission at longer wavelengths is expected. Overall, TTTMN is deemed the perfect choice for long-wavelength fluorescence imaging-guided PDT. The synthetic route of TTTMN is presented in Scheme S1 (Supporting Information), and the structures of intermediate and final products were characterized by ^{1}H NMR, ^{13}C NMR, and HRMS spectra (Figures S1–S9, Supporting Information).

First, the photophysical properties of TTTMN were studied. As depicted in **Figure 1a**, the maximum absorption of TTTMN in THF is ≈506 nm, and the PL spectrum of TTTMN in the solid state peaked at 746 nm with a quantum yield (QY) of 4.3%. As the PL spectrum is majorly located in the NIR region, TTTMN is a good imaging contrast agent for bioimaging. Then, the AIE feature of TTTMN was studied in THF/water mixtures with different water fractions (f_W). As shown in Figure 1b and S10, the PL intensities of TTTMN initially decrease from 0% to 50% owing to the twisted intramolecular charge transfer effect,[21] followed by a significant increase to 99% f_W due to the AIE effect. Specifically, the PL intensity of TTTMN in 99% f_W is 7.1 times higher than that in pure THF. The inset photo of TTTMN in 90% f_W is

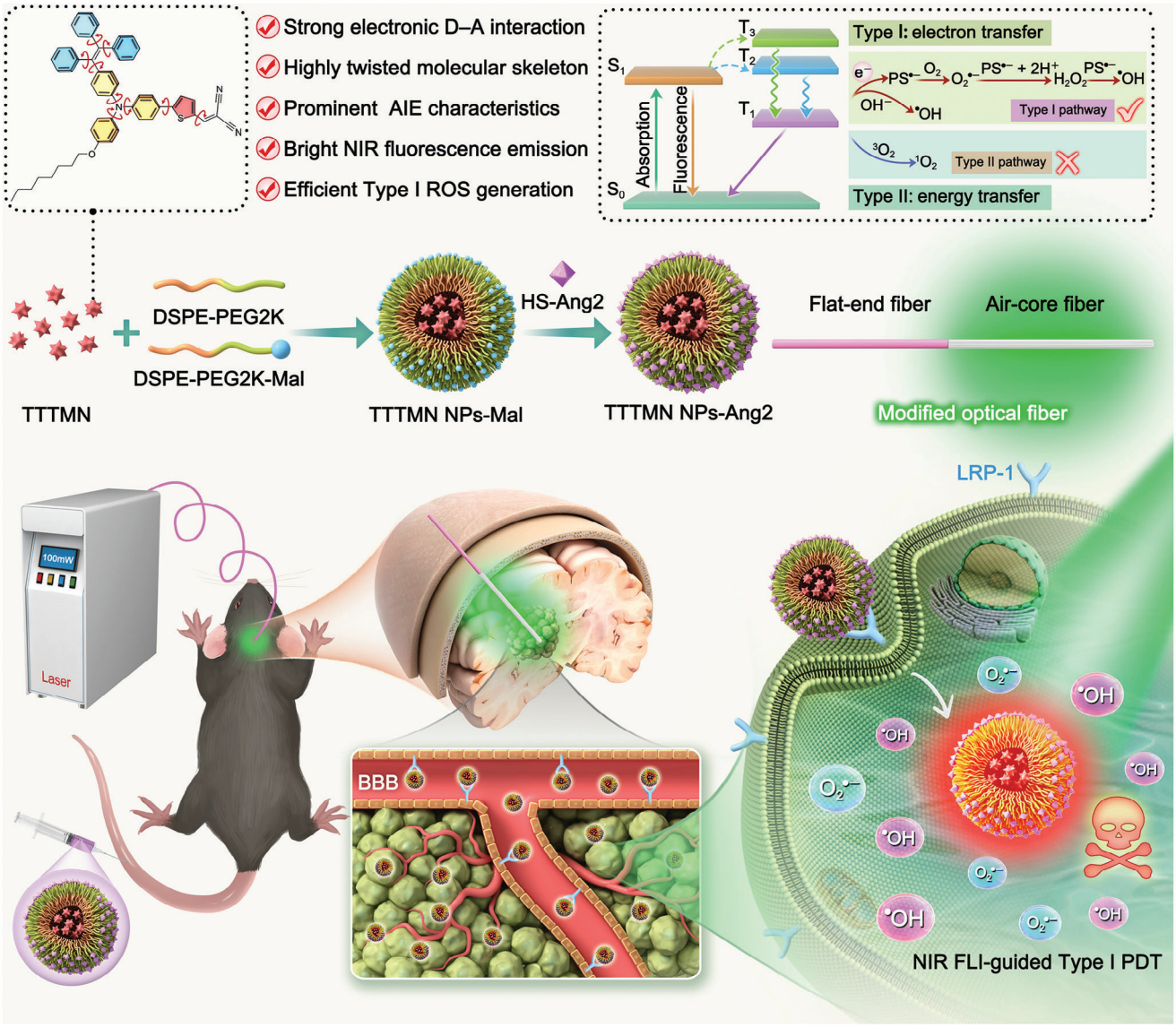

Scheme 1. Schematic illustration of molecular design principle, preparation of NPs, and fiber-optic mediated Type I PDT of brain GBM.

evidently brighter than that in 0% and 50% f_W. In addition, the QY of TTTMN in 0%, 50%, and 99% f_W were determined to be 0.87%, 0.41%, and 5.70%, respectively. These results clearly validated the AIE characteristics of TTTMN.

To render TTTMN with water dispersity and GBMs-targeting ability, NPs loaded with TTTMN were prepared based on a classical nanoprecipitation method followed by surface modification of Angiopep-2 (Ang2) via a click reaction.[22] The encapsulation efficiency of TTTMN was determined to be ≈89% (Figure S11, Supporting Information). Dynamic light scattering measurements show an increase in hydrodynamic size from 55.8 to 72.2 nm (Figure S12, Supporting Information and Figure 1c) and zeta potential from −3.16 to −1.07 eV (Figure S13, Supporting Information), respectively, confirming the successful modification of Ang2. TEM image shows that TTTMN NPs-Ang2 possess a spherical shape (Figure 1c). Next, the optical properties of TTTMN NPs-Ang2 were investigated. As shown in Figure 1d, TTTMN NPs-Ang2 exhibits an absorbance maximum at 520 nm and an emission peak at 722 nm. The PL spectrum of NPs overlaps with the NIR region well and the QY was determined to be 5.4%, benefiting the in vivo fluorescence imaging. Exceptionally, TTTMN NPs-Ang2 displayed remarkable photostability with negligible changes in absorbance after continuous laser irradiation of 30 min (200 mW cm^{-2}) (Figure S14, Supporting Information). In addition, TTTMN NPs-Ang2 also maintained their size, absorbance, and PL intensity in H_2O, PBS, and culture medium over 12 days, suggesting high stability (Figure S15, Supporting Information).

The photodynamic effect of TTTMN NPs-Ang2 was further evaluated. As shown in Figure 1e and Figure S16 (Supporting Information), the PL intensity of 2′,7′-dichlorodihydrofluorescein (DCFH) enhances sharply with increasing irradiation time in the presence of TTTMN NPs-Ang2, even with a low concentration of 1 μM. Notably, the fluorescence of DCFH reaches

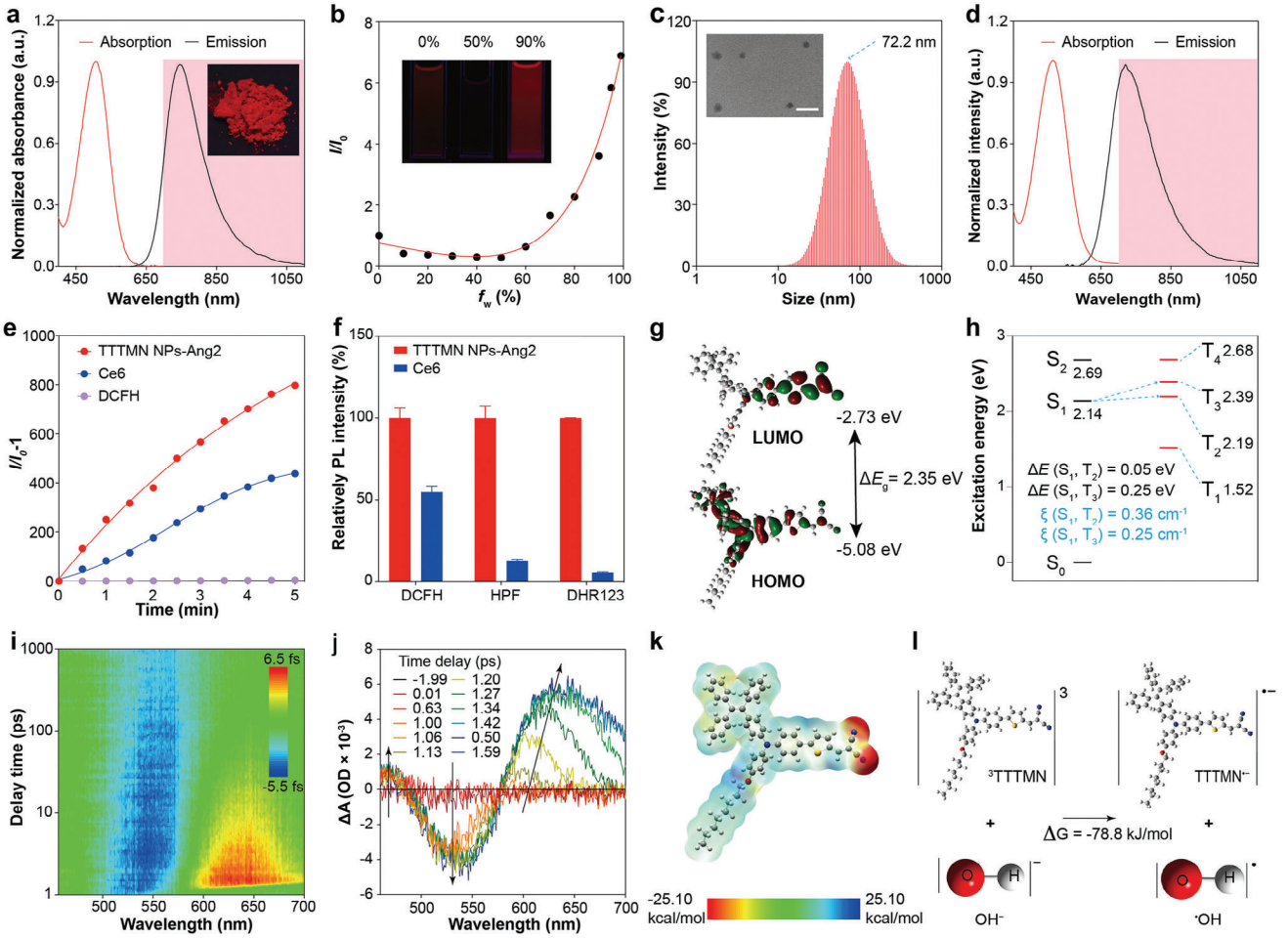

Figure 1. a) Normalized absorption of TTTMN in THF and normalized photoluminescence (PL) spectrum of TTTMN in the solid state. b) Plots of the relative emission intensity (I/I_0) versus f_W. I and I_0 are the PL peak values of TTTMN in the THF and THF/H_2O mixture, respectively. Inset photos show the fluorescence of TTTMN in 0%, 50%, and 90% mixture solvents. c) Size distribution and TEM image of TTTMN NPs-Ang2. Scale bar: 100 nm. d) Normalized absorption and PL spectra of TTTMN NPs-Ang2 in water. e) Photodynamic effect of TTTMN NPs-Ang2 under laser irradiation (520 nm, 100 mW). f) Relative yield of overall ROS, hydroxyl radicals, and superoxide radicals between TTTMN NPs-Ang2 and Ce6 (Mean ± SD, n = 3). g) Optimized S_0 geometry of TTTMN. h) Calculated energy gap and related spin-orbit coupling constants (ξ) of TTTMN based on S_0 structure at the level of PBE0/def2-TZVP. i) Contour plots of the time-resolved absorption spectroscopic responses. j) fs-TA spectra for TTTMN thin film. k) ESP mapped the molecular van der Waals surface of TTTMN. l) Gibbs free energy changes of electron transfer between TTTMN and hydroxyl anion.

≈800-fold after 6 min of irradiation, demonstrating the superior ROS production of TTTMN NPs-Ang2. Furthermore, the type of ROS generated by NPs was examined using various commercial indicators (hydroxyphenyl fluorescein: HPF for $OH^{\bullet}$; dihydrorhodamine: DHR 123 for $O_2^{\bullet-}$; 9,10-anthracenediyl-bis(methylene)dimalonic acid: ABDA for $^1O_2$). As shown in Figures S17–S19 (Supporting Information), HPF and DHR123 exhibit the highest fluorescence emission in the presence of TTTMN NPs-Ang2, while the degradation of ABDA is barely triggered, verifying their Type I ROS nature. Additionally, the ROS type generated by TTTMN NPs-Ang2 was confirmed by Electron Spin Resonance (ESR), which is consistent with the results mentioned above (Figure S20, Supporting Information).

To gain insight into the chemical structure of TTTMN, density functional theory (DFT) calculations were conducted. In Figure S21 (Supporting Information), large dihedral angles exceeding 60° are observed in the electron donor region, highlighting the torsional structure of TTTMN and its capacity to resist $\pi-\pi$ stacking upon aggregation. The molecular orbitals of TTTMN were further investigated. The HOMO is predominantly situated on the electron donor, while the LUMO is mainly distributed on the electron acceptor (Figure 1g), which illustrates the typical D–A interaction and signifies an effective internal charge transfer. The energy gap (ΔE_g) of TTTMN was calculated to be 2.35 eV. Time-dependent density functional theory (TD-DFT) was further employed to simulate the singlet and triplet states of TTTMN to assess its photodynamic potential. In Figure 1h, multiple energy transitions from S_1 to T_3 and T_2 have been assumed due to the narrow energy gap of 0.05 and 0.25 eV, respectively. Moreover, the spin-orbit coupling (SOC) values of these transitions were calculated to be 0.36 and 0.25 cm^{-1}, respectively. Such promising SOC values can be attributed to the substantial mixing of the wave functions between the lowest singlet charge transfer state (^{1}CT) and the local triplet excited state (^{3}LE), indicated by the natural

transition orbital (NTO) analyses (Figure S22, Supporting Information). The dense energy-level distributions and favorable SOC values establish a solid foundation for the efficient production of triplet excitons.

To gain a profound understanding of the triplet-involved process, the excited state properties of TTTMN were studied through femtosecond transient absorption (fs-TA) spectroscopy. The time-wavelength-dependent fs-TA color map offers a comprehensive visualization of the dynamic evolution of molecular excited states (Figure 1i). Two positive- and one negative-amplitude bands are observed within the pump-probe cross-correlation (Figure 1j). The negative-amplitude band corresponds to S_0 depopulation, in line with the absorption spectrum (Figure 1a), while the positive-amplitude bands indicate excited-state absorption (ESA) by transient species, with one band below 490 nm and the other peaking around 630 nm. These positive-amplitude absorption bands decay over a time range of ≈1.59 ps to 7.6 ns, concomitant with the observed S_0 repopulation (Figure S23, Supporting Information). Representative decay traces are reported in Figure S24 (Supporting Information). To assist in the assignment of TTTMN's transient species, the S_2, S_1, and T_1 states were optimized, and their ESAs were calculated (Figure S25, Supporting Information). The ESA reveals a significant overlap between the singlet states and the T_1 state, while the T_1 spectrum exhibits another distinct peak near 615 nm. The absorption below 490 nm is thus assigned to a combination of the singlet states and triplet manifold (i.e., T_3, T_2, and/or T_1), while the band between 580–700 nm is assigned to the triplet states. This is evident in Figure S24 (Supporting Information), where the kinetic traces at 471 nm increase before the increase of ESA at 635 nm. The instant growing of the 635 nm band also implies the efficient ISC from the singlet states to the triplet manifold. Additionally, this band redshifts within the pump-probe cross-correlation, indicating a molecular motion process of TTTMN.[23] These findings suggest the effective generation of T_1 states.

Additionally, the high electrophilicity of an electron acceptor is thought to enhance the electron transfer process, promoting type-I ROS generation. Hence, the electrostatic potential map (ESP) of TTTMN is calculated to visually illustrate the charge density distribution and identify potential reactive sites. As shown in Figure 1k, the negatively charged region predominantly concentrates on the cyano units, indicating highly reactive sites. Upon receiving an external electron, the acceptor moiety could disrupt the C≡N bond, producing radical anions (TTTMN$^{\bullet-}$), which can further transfer electrons to generate $O_2^{\bullet-}$ and $^{\bullet}$OH. The Gibbs free energy change (ΔG) of electron transfers was calculated to validate the feasibility. Specifically, the ΔG for the electron transfer process to $^3O_2$ with the generation of $O_2^{\bullet-}$ was determined to be −29.6 kcal mol^{-1}, and the ΔG for the electron transfer process to OH^- to yield $^{\bullet}$OH was calculated to be −78.8 kcal mol^{-1} (Figure 1l). These results manifest the feasibility of Type I ROS generation facilitated by TTTMN.

2.2. Design and Preparation of Optical Fiber for Light Delivery

To enable internal irradiation inside a tumor, a multimode optical fiber is modified by splicing with an air-core fiber and coating with epoxy resin (**Figure 2a**) to enhance light diffusion. Numerical simulations of the light field were implemented to optimize structure parameters. As shown in Figure 2b, increasing the air-core fiber diameter enhances light energy diffusion from the fiber end. Figure 2c further simulates the light transmission path, revealing that light diffusion results from multiple internal reflections and refractions. Guided by the simulation results, a series of optical fibers was prepared by splicing with air-core fibers of different diameters followed by coating of epoxy resin (Figure 2d). Then, the laser output power emitted from the fiber end was measured. The results in Figure 2e and Figure S26 (Supporting Information) confirm the simulations: greater output power is observed with larger air-core fiber diameters. Meanwhile, the epoxy resin coating can greatly increase the light diffusion extent at the fiber end, as demonstrated by the irradiation images of the optical fibers (Figure 2f). Noteworthy, with the largest diameter of the air-core fiber, the modified optical fiber exhibited almost 100% light emission at the fiber end. Hence, optical fiber spliced with 100 μm is chosen for the subsequent phototherapy.

The modified optical fiber was used to evaluate the ROS production of TTTMN NPs. As shown in Figures S27–S29 (Supporting Information), the relative PL intensity of ROS indicators increases gradually as the irradiation time is prolonged, similar to that of using a collimator. To demonstrate the superiority of the fiber, experiments were designed with mice skin and chicken breast tissue as the light barrier to simulate ROS generation in vivo (Figure 2g; Scheme S2, Supporting Information). As shown in Figure 2h, the relative PL intensity of DCFH increases significantly using a modified optical fiber. By contrast, the PL intensity of DCFH is barely increased using a collimator because only 10% of light can penetrate the skin layer. Moreover, the relative PL intensity of HPF and DHR123 are largely weakened using the collimator (Figure 2i). Then, chicken breast tissue with a thickness of 1 mm was used to simulate the biological tissue of mice. Similarly, strong PL intensities of ROS indicators are observed when irradiating samples with a modified optical fiber (Figure 2j). Chicken breast tissue poses a strong light barrier, blocks the incident light from the collimator, and results in a highly attenuated Type I ROS production (Figure 2k). Overall, the results mentioned above well-validate the potential of deep tissue PDT using a modified optical fiber.

2.3. Cellular Uptakes, Cytotoxicity Assay, and In Vitro Photodynamic Therapy

The oligopeptide Angiopep-2, known for its high blood-brain barrier (BBB) transcytosis capacity and glioblastoma (GBM)-targeting ability,[24] has been selected as the appropriate surface ligand to enhance the therapeutic efficacy of TTTMN NPs both in vitro and in vivo. Taking advantage of the fluorescence emission, flow cytometry is implemented to quantitatively evaluate and compare the cellular uptake of TTTMN NPs and TTTMN NPs-Ang2. As shown in **Figure 3a**, the mean fluorescence intensities (MFI) of GL261 are enhanced with increasing concentrations of NPs. As expected, the MFI of GL261 incubated with TTTMN NPs-Ang2 was significantly higher than that of TTTMN NPs at the same concentration. Such enhanced cellular uptakes were also confirmed at a wider range of concentrations (Figure S30, Supporting Information). Then, confocal laser scanning

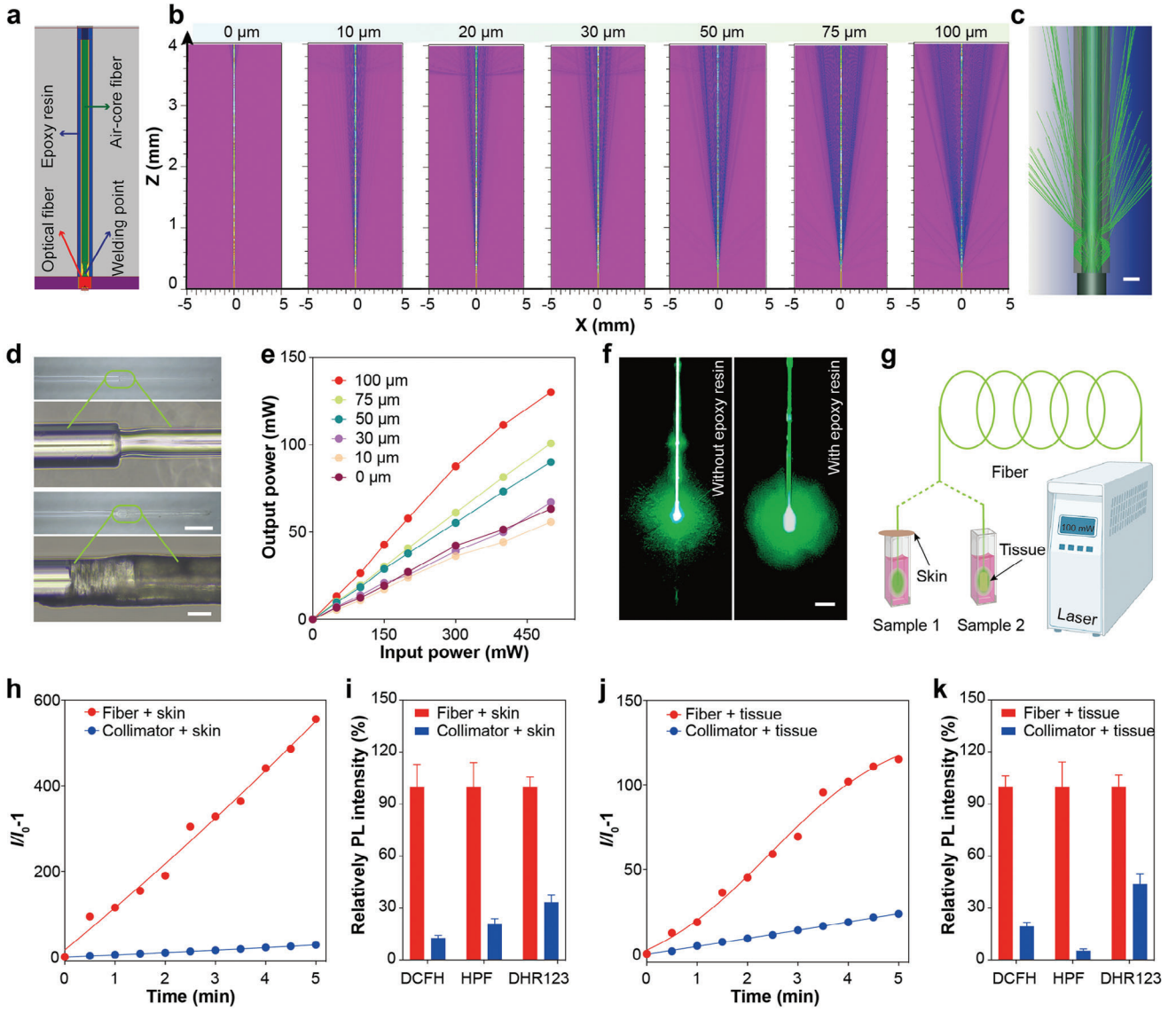

Figure 2. a) Schematic illustration demonstrates the structure of a modified optical fiber. Numerical simulation of b) light field and c) light transmission path emitted from the fiber end. Scale bar: 200 μm. d) Images of spliced optical fiber without and with epoxy resin coating. Scale bar: 1 mm and 100 μm. e) The power of light emitted from the fiber end with epoxy resin coating. f) Laser emission from the optimized modified optical fiber without and with epoxy resin coating. Scale bar: 3 mm. g) Schematic illustration of ROS generation irradiated by the optical fiber penetrating either skin or tissue. h) Plots of relative PL intensity ($I/I_0 - 1$) of DCFH and i) relatively PL intensity of different ROS indicators irradiated by a collimator or a modified optical fiber with skin as the light barrier (Mean ± SD, n = 3). j) Plots of relative PL intensity ($I/I_0 - 1$) of DCFH and k) Relatively PL intensity of different ROS indicators irradiated by collimator or a modified optical fiber with tissue as the light barrier (Mean ± SD, n = 3).

microscopy (CLSM) was adopted to visualize the cellular uptake of TTTMN NPs and TTTMN NPs-Ang2. As shown in Figure 3b and Figure S31 (Supporting Information), stronger red fluorescence was observed in GL261 cells incubated with TTTMN NPs-Ang2. These results solidly confirm the targeting ability of Ang-2 toward GL261 cells. Lastly, the endocytic pathways were assessed by employing various pathway inhibitors (Figure S32, Supporting Information). It is assumed that the internalization process of TTTMN NPs-Ang2 is energy-dependent, as evidenced by the significant reduction in cellular uptake at 4 °C and upon treatment with chlorpromazine (an inhibitor of clathrin-mediated endocytosis) and nystatin (an inhibitor of caveolae/lipid-mediated endocytosis) (Figure 3c). Notably, the inhibitory impact of chlorpromazine outweighed that of nystatin, suggesting the predominant involvement of the clathrin-mediated endocytosis pathway.

Encouraged by the efficient Type I ROS production of TTTMN NPs and the superiority of the modified optical fiber, the fiber optic-mediated PDT is subsequently assessed in vitro. First, the cytotoxicity of TTTMN NPs and TTTMN NPs-Ang2 are evaluated using four cell lines (human prostate cancer cell: PC3, glioma cell: GL261, human embryonic kidney: 293T, and human skin fibroblast cell: HS578BST). Figure 3d and Figures S33 and S34 (Supporting Information) show that cell survival rates were ≈90% across all concentrations (1–100 μM) and durations

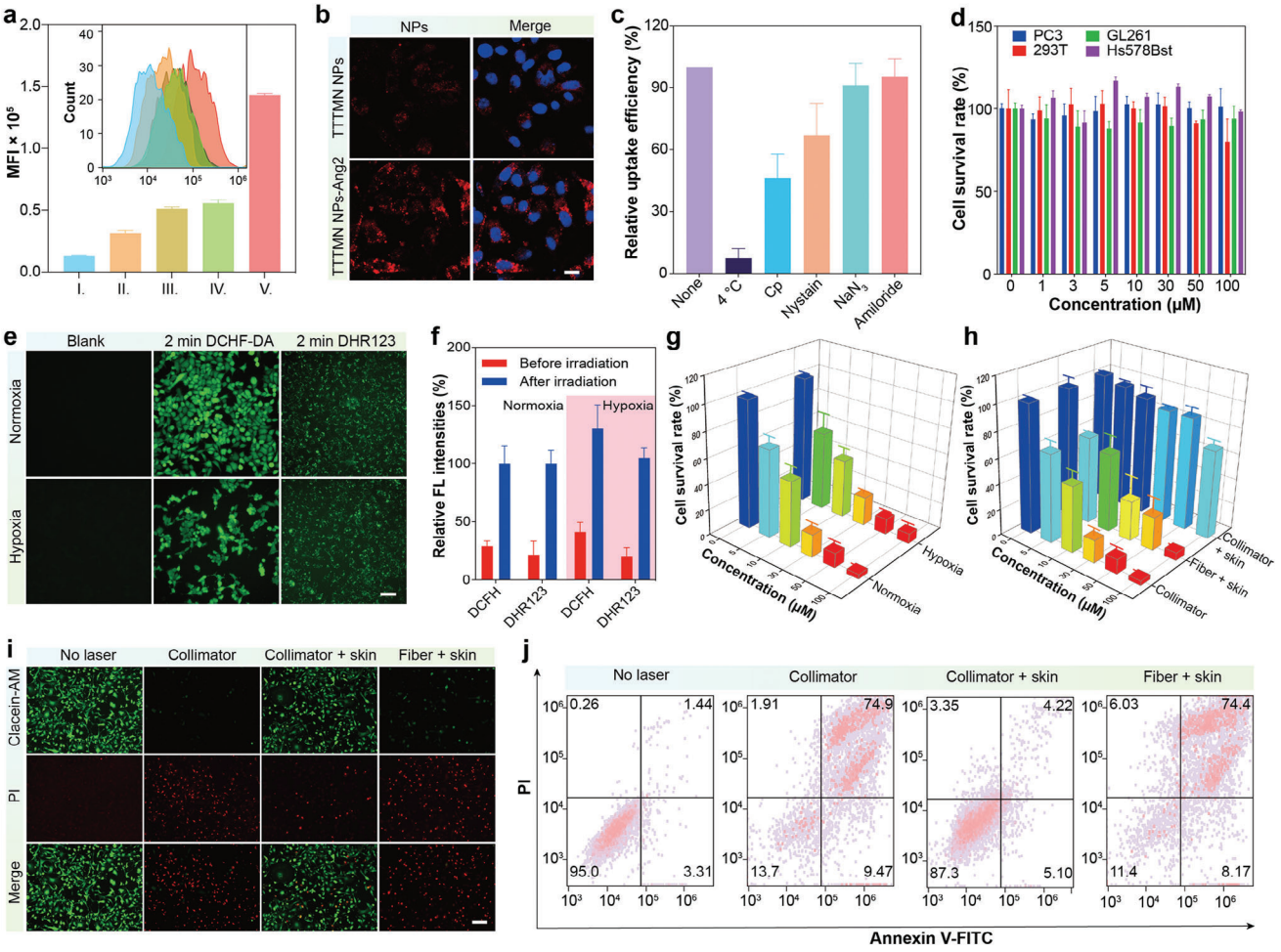

Figure 3. a) Flow cytometry analysis of cellular uptakes of TTTMN NPs and TTTMN NPs-Ang2. I: PBS; II: TTTMN NPs of 10 μM; III: TTTMN NPs-Ang2 of 10 μM; IV: TTTMN NPs of 50 μM; V: TTTMN NPs-Ang2 of 50 μM (Mean ± SD, n = 3). b) Intracellular localization of TTTMN NPs and TTTMN NPs-Ang2 (Concentration: 50 μM. Scale bar: 20 μm). c) Relative uptake efficiency of GL261 cells with different treatments. CP: chlorpromazine (Mean ± SD, n = 3). d) Cytotoxicity of TTTMN NPs-Ang2 after 24 h incubation (Mean ± SD, n = 3). e) Fluorescence images of GL261 staining with DCFH-DA and DHR123 in normoxic or hypoxic conditions with laser irradiation. Scale bars: 50 μm. f) Quantitative PL intensity of DCFH and DHR123 in normoxic or hypoxic conditions, respectively (Mean ± SD, n = 3). g) Cell survival rate of GL261 treated with TTTMN NPs-Ang2 mediated PDT in normoxic or hypoxic conditions (Mean ± SD, n = 3). (100 mW cm^{-2}, 20 min). h) Cell survival rate of GL261 treated with TTTMN NPs or TTTMN NPs-Ang2-mediated PDT irradiated by collimator or modified optical fiber (Mean ± SD, n = 3). i) Live/dead cell staining and j) apoptosis analysis of GL261 cells after various treatments (Scale bar: 100 μm).

(24–48 h), validating the biocompatibility and safety of TTTMN. Then, the intracellular ROS generation was examined by DCFH-DA and DHR123 in normoxic and hypoxic conditions in the presence of TTTMN NPs-Ang2 upon laser irradiation. As shown in Figure 3e, GL261 cells stained with DCFH-DA or DHR123 exhibit bright green fluorescence in both normoxic and hypoxic conditions, suggesting efficient ROS production even in a low-oxygen environment. By contrast, GL261 cells cultured under the same conditions without laser irradiation show negligible green fluorescence (Figure S35, Supporting Information). The FL intensities of DCFH and DHR123 were quantitatively summarized in Figure 3f, further demonstrating the Type I nature of TTTMN NPs-Ang2. CCK8 assay was further used to study the therapeutic effect of TTTMN NPs. As demonstrated in Figure S36 (Supporting Information), TTTMN NPs-Ang2 possesses much stronger efficacy than TTTMN NPs attributed to the enhanced cellular uptakes. Afterward, the therapeutic effect of TTTMN NPs-Ang2 against GL261 cells is explored at different oxygen content. Strikingly, similar cell survival rates of GL261 are obtained (Figure 3g), which indicates the remarkable therapeutic effect of TTTMN NPs-Ang2 in the tumor region. Furthermore, different irradiation methods were compared in vitro. GL261 cells treated with various concentrations of TTTMN NPs-Ang2 were irradiated by a collimator, a collimator with skin, and a modified optical fiber with skin (Scheme S3, Supporting Information), respectively. Figure 3h shows that TTTMN NPs-Ang2 can efficiently inhibit the growth of cancer cells after laser irradiation using either a collimator or a modified optical fiber. However, with the coverage of the mouse's skin, the treatment efficacy of collimator-mediated PDT is attenuated significantly, with over

68.7% of cells remaining alive even at a 100 μM concentration. By contrast, the fiber group can ignore the light obstruction of the skin, thereby maintaining a strong curative effect. The superiority of the modified optical fiber can also be convinced by the Calcein-AM/PI double staining results (Figure 3i; Figure S37, Supporting Information). In addition, GL261 cells remain vitality either in the absence of TTTMN NPs-Ang2 or laser irradiation, indicating the safety of TTTMN NPs-Ang2 and light delivery methods. Annexin V-FITC/PI assay is further used to clarify the cell death mechanism. Similar to the above results, cell apoptosis only appears in the collimator and fiber irradiation group (Figure 3j). By contrast, only a small part of cells endures apoptosis after laser irradiation via a collimator with skin.

2.4. In Vivo Photodynamic Therapy

The in *vivo* PDT of TTTMN NPs-Ang2 was further estimated. First, the biodistribution of TTTMN NPs-Ang2 in subcutaneous GBM models is investigated after intravenous injection with the dosage of 10 mg kg^{-1} to determine the optimal time for PDT. As shown in **Figure** 4a, distinct NIR fluorescence is observed at the tumor site with the maxima at 12 h postinjection of TTTMN NPs-Ang2 (Figure 4b; Figure S38, Supporting Information). Those results demonstrate the efficient tumor-targeting ability of TTTMN NPs-Ang2 and the therapeutic window for PDT. At 48 h postinjection, major organs of GBM-bearing mice were harvested for NIR imaging. As demonstrated in Figure S39 (Supporting Information), bright fluorescence signals majorly emit from tumor and liver tissues, confirming the good targeting ability of NPs and also implying the potential off-target effects on major organs. Then, the subcutaneous GBM-bearing mice were divided into 5 groups randomly (n = 5), including VI: PBS; VII: TTTMN NPs-Ang2; VIII: PBS + 520 nm laser via a modified optical fiber; IX: TTTMN NPs-Ang2 + 520 nm laser via a collimator; X: TTTMN NPs-Ang2 + 520 nm laser via a modified optical fiber. TTTMN NPs-Ang2 was administrated only once via intravenous injection, followed by one laser irradiation (520 nm, 100 mW, 20 min) at 12 h postinjection. In groups VIII and X, ≈3 mm of a modified optical fiber is located at the center region of tumors. A thorough inside-out laser irradiation at the tumor site is then observed according to Figure 4c. As demonstrated in Figure 4d, all the control groups (VI, VII, VIII) exhibit similar and growing patterns of tumor growth. By contrast, the tumor growth in group IX was inhibited to a relatively mild extent and significantly reduced tumor volume was observed in group X, proving the remarkable treatment efficacy of fiber optic-mediated Type I PDT. At the end of the treatment session, these tumors were dissected for weighing (Figure 4e; Figure S40, Supporting Information). Notably, group X exhibits the strongest inhibition of tumor growth compared with other groups ($P < 0.001$). Additionally, a negligible difference in the body weight of mice was observed among different groups during the therapeutic sessions (Figure S41, Supporting Information), indicating the safety of treatment.

Furthermore, cranial GBM models are established to study the targeting effect of TTTNM NPs-Ang2 toward orthotopic GBM (Figure S42, Supporting Information). As shown in Figure 4f, similar to that in the subcutaneous model, the maximum fluorescence is located at 12 h postinjection of NPs (Figure 4g; Figure S43, Supporting Information), indicating the optimal time for treatment and the BBB penetrating ability. Such an ability was further verified by the CLSM images of frozen brain tissue slides (Figure S44, Supporting Information). At 48 h postinjection, major organs and tumors of mice were harvested for fluorescence imaging. As shown in Figure S45 (Supporting Information), bright fluorescence signals still can be observed at the orthotopic GBM. Then, the tumoricidal effect of TTTMN NPs-Ang2 was assessed with irradiation using a modified optical fiber. Orthotopic GBM-bearing mice were divided randomly into the same 5 groups as previously mentioned. The therapeutic setup of PDT in orthotopic GBM models mediated by a modified optical fiber is shown in Figure 4h. The tumor growth status of orthotopic GBMs was recorded every two days using an IVIS-Spectrum living imaging system. As demonstrated in Figure 4i, the GBM growth in group X was entirely suppressed; however, the GBMs of other groups continuously grew throughout the treatment process. The corresponding quantitative bioluminescence intensities of GBMs are summarized in Figure 4j. These results highlighted the efficacy of Type I PDT of TTTMN NPs-Ang2 mediated by a modified optical fiber.

To gain insights into the therapeutic effect, GBMs are sliced perpendicular to the skin and stained for histological and immunohistochemical analyses 48 h after treatment. As shown in Figure 4k, the tumor section is not intact after PDT in group X, referring to a sign of severe cell damage. The detailed information is further provided by the enlarged view of H&E staining (Figure S46, Supporting Information), which shows increased cavities and conspicuous karyopyknosis. Remarkably, the TUNEL staining not only demonstrates the therapeutic effect of PDT but also indicates the illumination area inside the tumor. A clear boundary at the middle of the tumor is shown in group IX, implying that light cannot reach the deep inside of the tumor via a collimator. By sharp contrast, positive red signals are shown all over the tumor in group X, suggesting that the inside-out irradiation can counteract the light blockage of skin and tissue. Furthermore, the staining of tumors using Ki67 and CD31 exhibits similar patterns, in which the illumination area exhibits poor cell proliferation and angiogenesis.

Clearly, the proposed optical fiber-mediated Type I PDT offers a solution to the key challenges in conventional PDT, including the light blockage by biological tissues and the hypoxic environment within tumors. The main advantage of this photodynamic protocol is its ability to be safely administered to patients with deeply-seated and locally advanced tumors. Furthermore, this treatment can be repeated multiple times to achieve local control without causing long-term toxicity. These characteristics outperform traditional modalities such as surgery, chemotherapy, and radiotherapy. Hence, we are optimistic about the potential for this technique to become a standard clinical practice. Nevertheless, there are several aspects that warrant attention to enhance the feasibility of this technique. First, we recommend integrating in situ imaging or detection techniques into the photodynamic protocol to enable real-time dosimetry and optimize treatment outcomes. Second, it is essential to improve the strength and durability of the optical fiber further to ensure the reliability of this treatment approach. Lastly, enhancing the tumor-targeting capabilities of photosensitizers is crucial to minimize undesired side effects within the body.

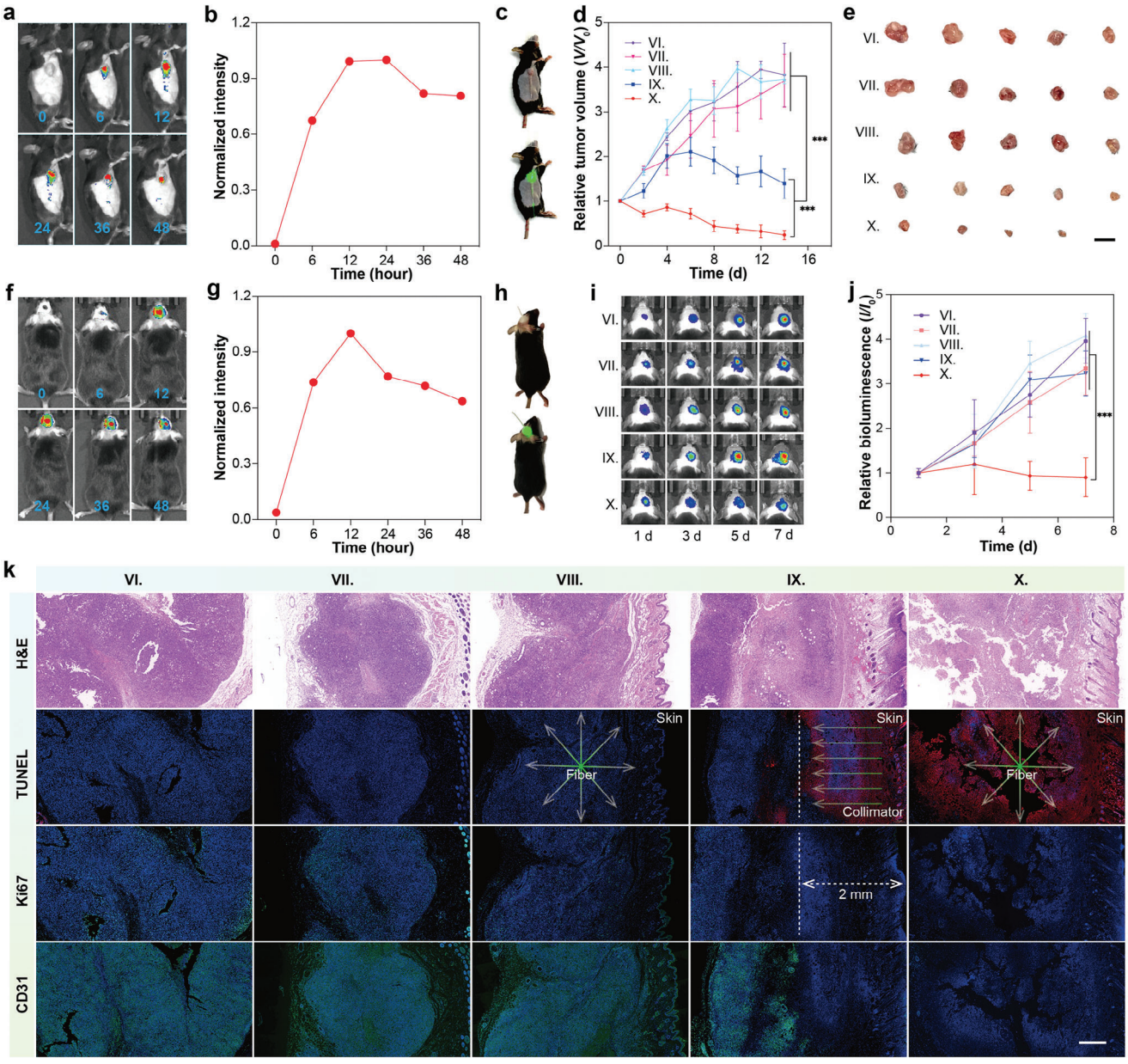

Figure 4. a) Fluorescence imaging and b) normalized FL intensities of subcutaneous GBM. c) The therapeutic setup of fiber optic-mediated PDT on subcutaneous GBM model mice. d) Subcutaneous GBM growth curves after various treatments during 14 days (Mean ± SD, n = 5, $p < 0.001$). e) Images of subcutaneous GBM after different treatments on day 14. Scale bar: 10 mm. f) Fluorescence imaging and g) normalized FL intensities of orthotopic GBM with cranial window. h) The therapeutic setup of fiber optic-mediated PDT on orthotopic GBM model mice. i) Bioluminescence images and j) relative bioluminescence intensity of orthotopic GBM-bearing mice with different treatments (Mean ± SD, n = 5, $p < 0.001$). k) Representative H&E, TUNEL, Ki67, and CD31-stained GBM tissue sections in different treatment groups. Scale bar: 0.5 mm. VI: PBS; VII: TTTMN NPs-Ang2; VIII: PBS + 520 nm laser via a modified optical fiber; IX: TTTMN NPs-Ang2 + 520 nm laser via a collimator; X: TTTMN NPs-Ang2 + 520 nm laser via a modified optical fiber.

2.5. Biosafety Assessments of TTTMN NPs-Ang2

The biosafety of NPs is an essential factor in clinical application, the systemic toxicity of TTTMN NPs-Ang2 was thus comprehensively studied using various evaluation methods. A hemolysis test of TTTNM NPs-Ang2 was conducted to assess the blood biocompatibility at different concentrations ranging from 1 to 100 µM before in vivo assessments. As shown in Figure S47 (Supporting Information), negligible hemolysis is obtained in all test concentrations, and positive hemolysis is obtained using deionized water. Such results display that TTTNM NPs-Ang2 are safe for red blood cells and suitable for intravenous injection. Subsequently, healthy BALB/c mice are treated with 10 mg kg^{-1} TTTNM NPs-Ang2 serving as experiment groups or 100 µL PBS serving as blank control. The body weight change of the two groups of mice is not diverse over two weeks of feeding

(Figure S48, Supporting Information), suggesting that NPs would not cause acute biological toxicity at this therapeutic dose. Within the 15 days of the experiment, no noticeable differences in body shape, weight, eating, defecating, and activity have been observed. On day 15, blood routine and biochemistry index analyses of treated mice were performed. As shown in Figures S49 and S50 (Supporting Information), all the indexes are located at healthy levels, implying TTTMN NPs-Ang2 would not interrupt the liver and kidney functions and the immune system. Then, the organ coefficient (Figure S51, Supporting Information) and H&E-stained slices (Figure S52, Supporting Information) of the main organs (heart, liver, spleen, lung, and kidney) collected from treated mice have no difference in pathology, further confirming the safety use of TTTMN NPs-Ang2. Therefore, it can be concluded that TTTMN NPs-Ang2 possess excellent biocompatibility and biosafety, holding convincingly potential in clinical PDT.

3. Conclusion

In this contribution, a fiber optic-mediated Type I PDT is proposed for the first time to combat brain GBMs in vivo using a modified optical fiber and a prominent Type I AIE PS. By integrating multiple molecular rotors, a sterically encumbered alkyl chain, and a strong D–A interaction, TTTMN demonstrates a notable AIE effect and a high production rate of Type I ROS upon aggregation. The experimental and theoretical studies disclose that the multi-channel transitions and the electrophilicity of the acceptor collectively lead to the outstanding Type I photodynamic effects of NPs. After being formulated into NPs and modified with Ang2, TTTMN NPs-Ang2 can efficiently penetrate the BBB and selectively target GBMs. Outstanding therapeutic effect in vivo is observed after laser irradiation through a modified optical fiber, which is inserted into the GBMs after penetrating the light barriers of skin, skull, and tissues. Overall, this work opens up new avenues for GBM treatment by taking advantage of both optical fiber and less oxygen-dependent Type I PS, surely advancing the clinical application of PDT.

4. Experimental Section

Fabrication of Modified Optical Fiber: The diameter of the fiber core with the cladding coating of 220 µm. Air-core fiber with 0, 10, 20, 30, 50, 75, and 100 µm aperture were purchased from Fiber Optics Solutions company. At first, the polyimide coating of two types of optical fibers was peeled off. Then, two types of optical fibers were fixed on the fusion splicer. The air-core fiber was manually directed to the center of the flat-end conventional optical fiber in good alignment. Splicing parameters: cleaning discharge time: 40 ms; fiber pre-melting time: 180 ms; fiber pre-melting power: standard; discharge time: 1500 ms; discharge power: standard. After splicing, only 2–3 mm long air-core fiber was retained by cutting off the residual. UV-curable epoxy resin with a refractive index of 1.6 was further coated on the surface of the air-core fiber followed by UV irradiation. The epoxy resin coating was then polished to a thickness of ≈50 µm. The as-prepared modified optical fiber was characterized by a stereo microscope and an inverted microscope. When the input power is 0, 100, 200, 300, 400, or 500 mW, the laser from the side surfaces of the modified optical fiber coated without or with epoxy resin is measured by an optical power meter.

Establishment of Subcutaneous GBM Model: The abdominal hair of 6-week-old C57 mice was depilated one day in advance, and 100 µL of Matrigel containing 1 million GL261 cells was implanted into the right forelimb armpit. After ≈7 days, tumor volume has increased to approximately volume of 80–100 mm^3. Tumor volume was calculated using the following Equation (1):[25]

$$\text{Volume} = \text{length} \times \text{width}^2 \quad (1)$$

Establishment of Orthotopic GBM Model: Establishment of orthotopic GBM model. Mice placed on a heating pad were anesthetized using isoflurane, and placed in a stereotaxic frame. The head was depilated by a shaver and applying hair removal cream. Then a small hole in the right skull was made using a special needle. Considering intracranial orthotopic GBM can't be directly observed by naked eyes, luciferase labeled GL261 (GL261-LUC) was used to establish the orthotopic GBM model, which growth status of the tumor can be obtained by bioluminescence using IVIS-Spectrum living imaging system. 10 µL of Matrigel containing 1 $\times 10^5$ GL261-LUC cells were implanted into the brain at a rate of 10 µL min^{-1} by the small hole using a micro-pump-controlled Hamilton syringe. The depth of implantation was 2 mm. After 7 days, the orthotopic GBM tumor can be observed by IVIS-Spectrum living imaging system after 10 min postinjection of D-Luciferin sodium salt with 0.1 mg g^{-1} dose.

In Vivo PDT: Tumor-bearing mice were randomly divided into 5 groups (N = 5), including VI: PBS; VII: TTTMN NPs-Ang2; VIII: PBS plus 520 nm laser via a modified optical fiber; IX: TTTMN NPs-Ang2 plus 520 nm laser via a collimator; X: TTTMN NPs-Ang2 plus 520 nm laser via a modified optical fiber. Each mouse was intravenously injected with samples with a dose of 10 mg kg^{-1} and a volume of ≈100 µL. The control group was injected with 100 µL of PBS. Then, at 12 h post-injection, the mice were anesthetized using 2% isoflurane in oxygen and fixed on a heating pad. The tumor of mice in group IX was irradiated by a 520 nm laser (100 mW cm^{-2}) with a collimator for 20 min. The tumor of mice in groups VIII and X was irradiated with a modified optical fiber with the same parameters.

For orthotopic GBM-bearing mice, a small hole on the right skull was made using a special needle in groups VIII and X. Then, the fiber was implanted into a depth 2 of mm through the small hole. Tumor growth status is characterized using in vivo fluorescence imaging. For subcutaneous GBM, the fiber of 3 mm length was accurately implanted through an indwelling needle into the center in groups VIII and X. The body weight and tumor volume were recorded once every two days. To analyze the therapeutic outcomes of phototherapy, tumors were harvested from one of the mice in each group at 24 h post-irradiation to implement histopathological analyses. The sections were then subjected to H&E, CD31, Ki67, and TUNEL staining for histopathological analysis. The tissue slices were imaged by an inverted optical microscopy.

Animal Ethics: The protocol of animal experiments was approved by the Animal Ethical and Welfare Committee of Shenzhen University (AEWC-SZU, AEWC-202300019) in China, and the experiments were performed strictly according to governmental and international guidelines on animal experimentation. According to requirements for Biosafety and Animal Ethics, all efforts were made to minimize the number of animals used and their suffering.

Statistical Analysis: Normalization and evaluation of outliers were used to pre-process data when needed. Data were presented as means ± SD. The sample size for each statistical analysis is either n = 3 or n = 5 as indicated in the manuscript. The statistical significance was examined by Student's *t*-test when two groups were compared. Statistical analysis considered significant differences when P values < 0.05. Statistical analysis was performed using ANOVA.

Supporting Information

Supporting Information is available from the Wiley Online Library or from the author.

Acknowledgements

W.Z. and M.K. contributed equally to this work. The authors acknowledge the financial support from the National Natural Science Foundation of

China (62205216, 22105130, 22275124, 52122317), the Basic and Applied Basic Research Foundation of Guangdong Province (2022A1515010381), the Basic Research Foundation of Shenzhen (JCYJ20220531101814034, JCYJ20230808105412024), Supported by the Medicine Plus Program of Shenzhen University (2023YG002, 2024YG009), the Scientific Instrument Developing Project of Shenzhen University (2023YQ008), and Start-up Grant from Shenzhen University (868-000001032015, 868–000001032219, 868–000001032113). The authors also thank the Instrument Analysis Centre of Shenzhen University for the equipment used.

Conflict of Interest

The authors declare no conflict of interest.

Data Availability Statement

The data that support the findings of this study are available from the corresponding author upon reasonable request.

Keywords

aggregation-induced emission, brain glioblastoma, optical fiber, photodynamic theranostics, Type I photosensitizer

Received: July 14, 2024
Revised: September 20, 2024
Published online:

[1] a) L. R. Schaff, I. K. Mellinghoff, *JAMA, J. Am. Med. Assoc.* **2023**, *329*, 574; b) J. H. Sampson, M. D. Gunn, P. E. Fecci, D. M. Ashley, *Nat. Rev. Cancer* **2020**, *20*, 12.

[2] a) L. Hua, Z. Wang, L. Zhao, H. Mao, G. Wang, K. Zhang, X. Liu, D. Wu, Y. Zheng, J. Lu, R. Yu, H. Liu, *Theranostics* **2018**, *8*, 5088; b) A. De Boeck, B. o. Y. Ahn, C. D'Mello, X. Lun, S. V. Menon, M. M. Alshehri, F. Szulzewsky, Y. Shen, L. Khan, N. H. Dang, E. Reichardt, K.-A. Goring, J. King, C. J. Grisdale, N. Grinshtein, D. Hambardzumyan, K. M. Reilly, M. D. Blough, J. G. Cairncross, V. W. Yong, M. A. Marra, S. J. M. Jones, D. R. Kaplan, K. D. McCoy, E. C. Holland, P. Bose, J. A. Chan, S. M. Robbins, D. L. Senger, *Nat. Commun.* **2020**, *11*, 4997.

[3] X. Peng, X. Huang, S. Zhang, N. Zhang, S. Huang, Y. Wang, Z. Zhong, S. Zhu, H. Gao, Z. Yu, X. Yan, Z. Tao, Y. Dai, Z. Zhang, X. Chen, F. Wang, F. X. Claret, M. Elkabets, N. Ji, Y. Zhong, D. Kong, *Adv. Sci.* **2024**, *11*, 2307747.

[4] a) S. Son, C. Zhang, M. Won, P. Jangili, M. Choi, J. Wu, J. S. Kim, *Aggregate* **2021**, *2*, e97; b) A. Salvalaggio, L. Pini, A. Bertoldo, M. Corbetta, *Lancet Neurol.* **2024**, *23*, 740.

[5] a) H.-A. Leroy, G. Baert, L. Guerin, N. Delhem, S. Mordon, N. Reyns, A.-S. Vignion-Dewalle, *Cancers* **2021**, *13*, 5754; b) A. Omuro, L. M. DeAngelis, *JAMA, J. Am. Med. Assoc.* **2013**, *310*, 1842.

[6] a) T. Hsia, J. L. Small, A. Yekula, S. M. Batool, A. K. Escobedo, E. Ekanayake, D. G. You, H. Lee, B. S. Carter, L. Balaj, *Cancers* **2023**, *15*, 3918; b) Y. Chen, Y. Ma, K. Shi, H. Chen, X. Han, C. Wei, Y. Lyu, Y. Huang, R. Yu, Y. Song, Q. Song, J. Jiang, J. Feng, Y. Lin, J. Chen, H. Chen, G. Zheng, X. Gao, G. Jiang, *Adv. Mater.* **2024**, *36*, 2307454; c) D. B. L. Teh, A. Bansal, C. Chai, T. B. Toh, R. A. J. Tucker, G. G. L. Gammad, Y. Yeo, Z. Lei, X. Zheng, F. Yang, J. S. Ho, N. Bolem, B. C. Wu, M. K. Gnanasammandhan, L. Hooi, G. S. Dawe, C. Libedinsky, W.-Y. Ong, B. Halliwell, E. K.-H. Chow, K.-L. Lim, Y. Zhang, B. K. Kennedy, *Adv. Mater.* **2020**, *32*, 2001459.

[7] H.-Z. Xu, T.-F. Li, Y. Ma, K. Li, Q. Zhang, Y.-H. Xu, Y.-C. Zhang, L. Zhao, X. Chen, *Biomaterials* **2022**, *290*, 121833.

[8] a) I. Kirino, K. Fujita, K. Sakanoue, R. Sugita, K. Yamagishi, S. Takeoka, T. Fujie, S. Uemoto, Y. Morimoto, *Sci. Rep.* **2020**, *10*, 22017; b) M. D. Caverzán, P. M. Oliveda, L. Beaugé, R. E. Palacios, C. A. Chesta, L. E. Ibarra, *Cells* **2023**, *12*, 1541; c) A. Abdurashitov, V. Tuchin, O. Semyachkina-Glushkovskaya, *J. Innov. Opt. Health Sci.* **2020**, *13*, 2030004; d) W. S. Kim, M. I. Khot, H.-M. Woo, S. Hong, D.-H. Baek, T. Maisey, B. Daniels, P. L. Coletta, B.-J. Yoon, D. G. Jayne, S. I. l. Park, *Nat. Commun.* **2022**, *13*, 2178.

[9] a) M. Fan, Z. Xu, M. Liu, Y. Jiang, X. Zheng, C. Yang, W.-C. Law, M. Ying, X. Wang, Y. Shao, M. T. Swihart, G. Xu, K.-T. Yong, B. Z. Tang, *Appl. Phys. Rev.* **2021**, *8*, 041328; b) Y. Jiang, W. Zhu, Z. Xu, Z. Zhang, S. Tang, M. Fan, Z. Li, J. Zhang, C. Yang, W.-C. Law, K.-T. Yong, D. Wang, G. Xu, B. Zhong Tang, *Chem. Eng. J.* **2022**, *448*, 137604; c) Z. Xu, Y. Jiang, Y. Shen, L. Tang, Z. Hu, G. Lin, W.-C. Law, M. Ma, B. Dong, K.-T. Yong, G. Xu, Y. Tao, R. Chen, C. Yang, *Mater. Horiz.* **2022**, *9*, 1283.

[10] a) R. Wang, X. Li, L. Zhou, F. Zhang, *Angew. Chem., Int. Ed.* **2014**, *53*, 12086; b) H. Yi, D. Ghosh, M.-H. Ham, J. Qi, P. W. Barone, M. S. Strano, A. M. Belcher, *Nano Lett.* **2012**, *12*, 1176.

[11] a) J. Gao, Z. Chen, X. Li, M. Yang, J. Lv, H. Li, Z. Yuan, *Int. J. Mol. Sci.* **2022**, *23*, 12556; b) K. Deng, C. Li, S. Huang, B. Xing, D. Jin, Q. Zeng, Z. Hou, J. Lin, *Small* **2017**, *13*, 1702299.

[12] W. Zhang, X. Li, M. Kang, Z. Zhang, Y. u. Pei, M. Fan, D. Yan, Y. Zhang, C. Yang, G. Xu, D. Wang, Z. Xu, B. Z. Tang, *ACS Mater. Lett.* **2024**, *6*, 2174.

[13] a) X. Li, N. Kwon, T. Guo, Z. Liu, J. Yoon, *Angew. Chem., Int. Ed.* **2018**, *57*, 11522; b) Q. Li, A. Wang, J. Li, S. Liang, Y. Tian, S. Bai, *Matter* **2022**, *5*, 2425; c) Z. Yang, J. Wang, S. Ai, J. Sun, X. Mai, W. Guan, *Theranostics* **2019**, *9*, 6809.

[14] a) Z. Shen, Q. Ma, X. Zhou, G. Zhang, G. Hao, Y. Sun, J. Cao, *NPG Asia Mater* **2021**, *13*, 39; b) I. S. Turan, D. Yildiz, A. Turksoy, G. Gunaydin, E. U. Akkaya, *Angew. Chem., Int. Ed.* **2016**, *55*, 2875; c) R.-Q. Li, C. Zhang, B.-R. Xie, W.-Y. Yu, W.-X. Qiu, H. Cheng, X.-Z. Zhang, *Biomaterials* **2019**, *194*, 84.

[15] Y. Ran, Z. Xu, M. Chen, W. Wang, Y. Wu, J. Cai, J. Long, Z. Chen, D. Zhang, B. Guan, *Adv. Sci.* **2022**, *9*, 2200456.

[16] A. L. Chin, S. Jiang, E. Jang, L. Niu, L. Li, X. Jia, R. Tong, *Nat. Commun.* **2021**, *12*, 5138.

[17] a) Z. Zhuang, J. Dai, M. Yu, J. Li, P. Shen, R. Hu, X. Lou, Z. Zhao, B. Z. Tang, *Chem. Sci.* **2020**, *11*, 3405; b) Z. Meng, H. Xue, T. Wang, B. Chen, X. Dong, L. Yang, J. Dai, X. Lou, F. Xia, *J. Nanobiotechnol.* **2022**, *20*, 344.

[18] a) Q. Yao, J. Fan, S. Long, X. Zhao, H. Li, J. Du, K. Shao, X. Peng, *Chem* **2022**, *8*, 197; b) R. Lin, J. Liu, W. Xu, Z. Liu, X. He, C. Zheng, M. Kang, X. Li, Z. Zhang, H.-T. Feng, J. W. Y. Lam, D. Wang, M. Chen, B. Z. Tang, *Adv. Mater.* **2023**, *35*, 2303212.

[19] a) S. Zhang, P. Zhang, B. Z. Tang, *Aggregate* **2024**, *5*, e605; b) Z. Zhang, M. Kang, H. Tan, N. Song, M. Li, P. Xiao, D. Yan, L. Zhang, D. Wang, B. Z. Tang, *Chem. Soc. Rev.* **2022**, *51*, 1983; c) T. C. Pham, V.-N. Nguyen, Y. Choi, S. Lee, J. Yoon, *Chem. Rev.* **2021**, *121*, 13454; d) X. Zhao, J. Liu, J. Fan, H. Chao, X. Peng, *Chem. Soc. Rev.* **2021**, *50*, 4185.

[20] a) P. Cen, J. Huang, C. Jin, J. Wang, Y. Wei, H. Zhang, M. Tian, *Aggregate* **2023**, *4*, e352; b) H. Yu, B. Chen, H. Huang, Z. He, J. Sun, G. Wang, X. Gu, B. Z. Tang, *Biosensors* **2022**, *12*, 348; c) Y. Tang, Y. Li, B. Li, W. Song, G. Qi, J. Tian, W. Huang, Q. Fan, B. Liu, *Nat. Commun.* **2024**, *15*, 2530; d) Q. He, M. Wang, L. Zhao, B. Xu, W. Tian, L. Zhang, *Aggregate* **2024**, *5*, e615.

[21] a) J. Li, J. Wang, J. Zhang, T. Han, X. Hu, M. M. S. Lee, D. Wang, B. Z. Tang, *Adv. Mater.* **2021**, *33*, 2105999; b) S. Gao, G. Wei, S. Zhang, B. Zheng, J. Xu, G. Chen, M. Li, S. Song, W. Fu, Z. Xiao, W. Lu, *Nat. Commun.* **2019**, *10*, 2206; c) C. Wang, Q. Qiao, W. Chi, J. Chen, W. Liu, D. Tan, S. McKechnie, D. a. Lyu, X.-F. Jiang, W. Zhou, N. Xu, Q. Zhang, Z. Xu, X. Liu, *Angew. Chem., Int. Ed.* **2020**, *59*, 10160.

[22] a) J. Zhang, K. Wei, J. Shi, Y. Zhu, M. Guan, X. Fu, Z. Zhang, *ACS Biomater. Sci. Eng.* **2021**, *7*, 1496; b) S. Habib, M. Singh, *Polymers* **2022**, *14*, 712.
[23] H. Zhang, J. Liu, L. Du, C. Ma, N. L. C. Leung, Y. Niu, A. Qin, J. Sun, Q. Peng, H. H. Y. Sung, I. D. Williams, R. T. K. Kwok, J. W. Y. Lam, K. S. Wong, D. L. Phillips, B. Z. Tang, *Mater. Chem. Front.* **2019**, *3*, 1143.
[24] a) B. Oller-Salvia, M. Sánchez-Navarro, E. Giralt, M. Teixidó, *Chem. Soc. Rev.* **2016**, *45*, 4690; b) Y. Jiang, W. Yang, J. Zhang, F. Meng, Z. Zhong, *Adv. Mater.* **2018**, *30*, 1800316; c) J. Liu, Y. Sun, X. Zeng, Y. Liu, C. Liu, Y. Zhou, Y. Liu, G. Sun, M. Guo, *Adv. Mater.* **2023**, *35*, 2303660.
[25] M. Li, M. Wang, J. Huang, S. Tang, J. Yang, Z. Xu, G. Xu, X. Chen, J. Liu, C. Yang, *J. Nanobiotechnol.* **2024**, *22*, 141.